

FIG. S1. **Coordinate system and axes conventions for simulating montage data collection.** All simulations use the standard right-handed Cartesian coordinate system, with the origin at the center of the specimen (blue rectangular prism). The specimen is tilted around the x -axis. A tilt angle α is positive if the specimen is tilted counterclockwise when viewed from the positive side of the x -axis. An electron beam (yellow cylinder) is delivered to the specimen along the z -axis from the positive side. The illuminated volume of the specimen is the cylinder outlined by the orange ellipses. In projection the beam is circular at the first tilt angle of 0° and becomes increasingly elliptical at higher tilt angles, with the long axis of the ellipse aligned with the y -axis of the detector.

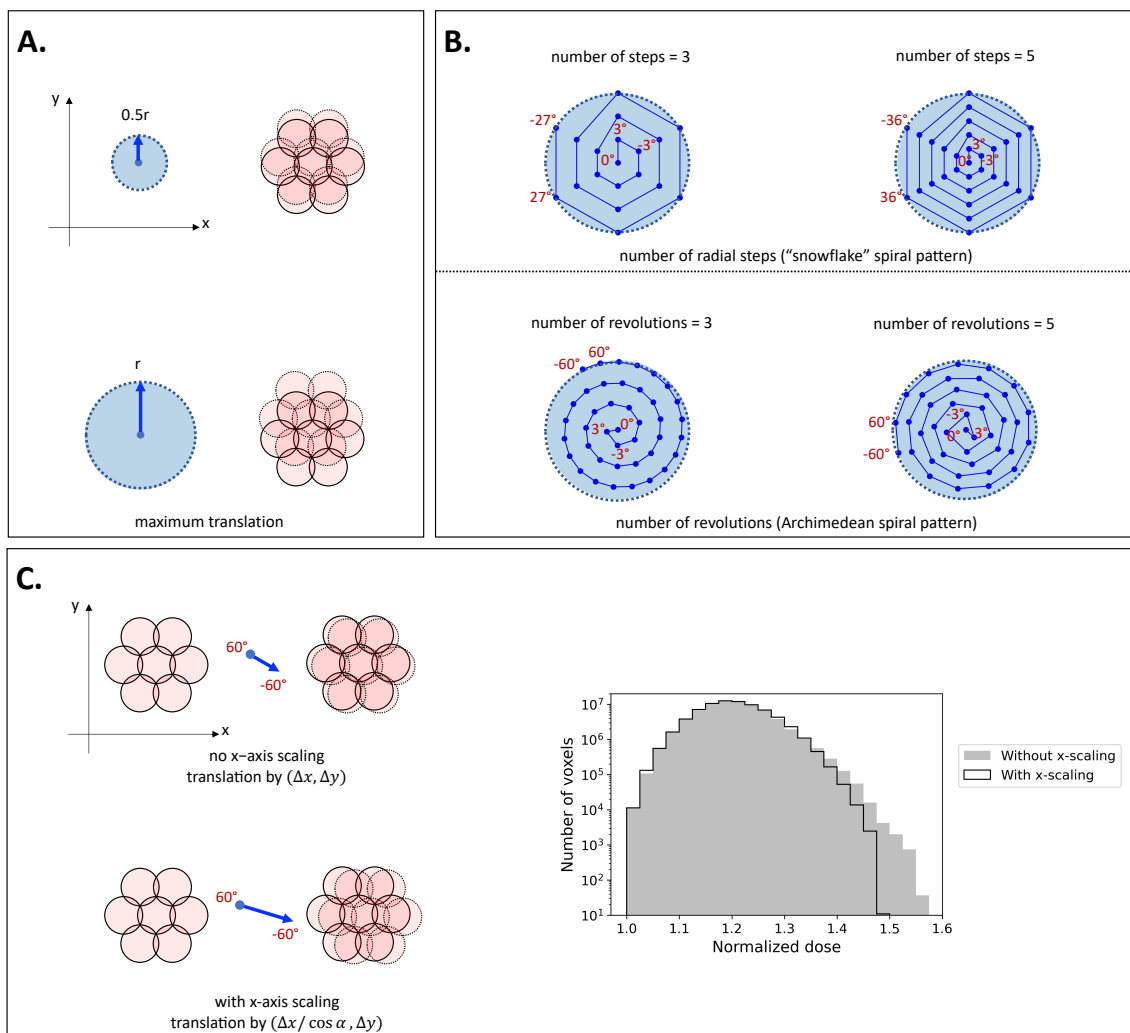


FIG. S2. Global translational offsets of the tiling pattern change which regions of the specimen are imaged more than once at each tilt angle. For visual clarity, only the central seven tiles (pink circles) are shown. Solid and dashed borders respectively indicate tile positions before and after the indicated translation has been applied between successive tilt angles. The following parameters were varied to determine the combination of translations that optimized the efficiency of the distributed dose. (A) Maximum translation: the maximum displacement allowed for any tile during the tilt-series was varied from 0 (no offsets) to r (one beam radius). The blue circles on the left demarcate the region of allowed shifts for the central tile for a maximum translation of $0.5r$ (top) and r (bottom). The change in the overlap region for a translation of this magnitude along the y -axis of the detector is shown on the right. (B) Number of radial steps / number of revolutions: both parameters specify how tightly packed the spiral pattern is. Each blue dot represents the position of the central tile after the translational offset is applied at each tilt angle. The large light blue circles represent the region of allowed displacement as described in (A). For the snowflake pattern (top), the number of radial steps is the number of points between the center and edge of the light blue circle along any of the six translational directions. If the maximum translation is reached before the final tilt angle of -60° , the translational offsets for the remaining tilt angles repeat the snowflake pattern starting from the center. Archimedean spiral patterns avoid this issue by fitting all tilt angles into the light blue circles regardless of the number of revolutions (bottom). (C) Optional x -axis translational scaling: the x -axis component of all translations is optionally scaled by the cosine of the current tilt angle. The difference is subtle and most evident between tilt angles of 60° and -60° , as shown on the left, where with scaling (lower) the x -axis translational offset is twice that without scaling (upper). This scaling is motivated by the elliptical projection of the beam at high tilt angles, with the long-axis of the ellipse aligned with the y -axis (Fig. S1). As a result of the elliptical projections, regions of the specimen that were previously in the overlap region are more likely to be in the overlap region again along the y -axis than x -axis. To compensate for this, application of an additional x -axis translation that mirrored the elongation of the elliptical projection was tested. As shown by the overlaid histograms on the right, x -axis scaling reduced the number of voxels in the specimen that received high dose for a basic spiral pattern.

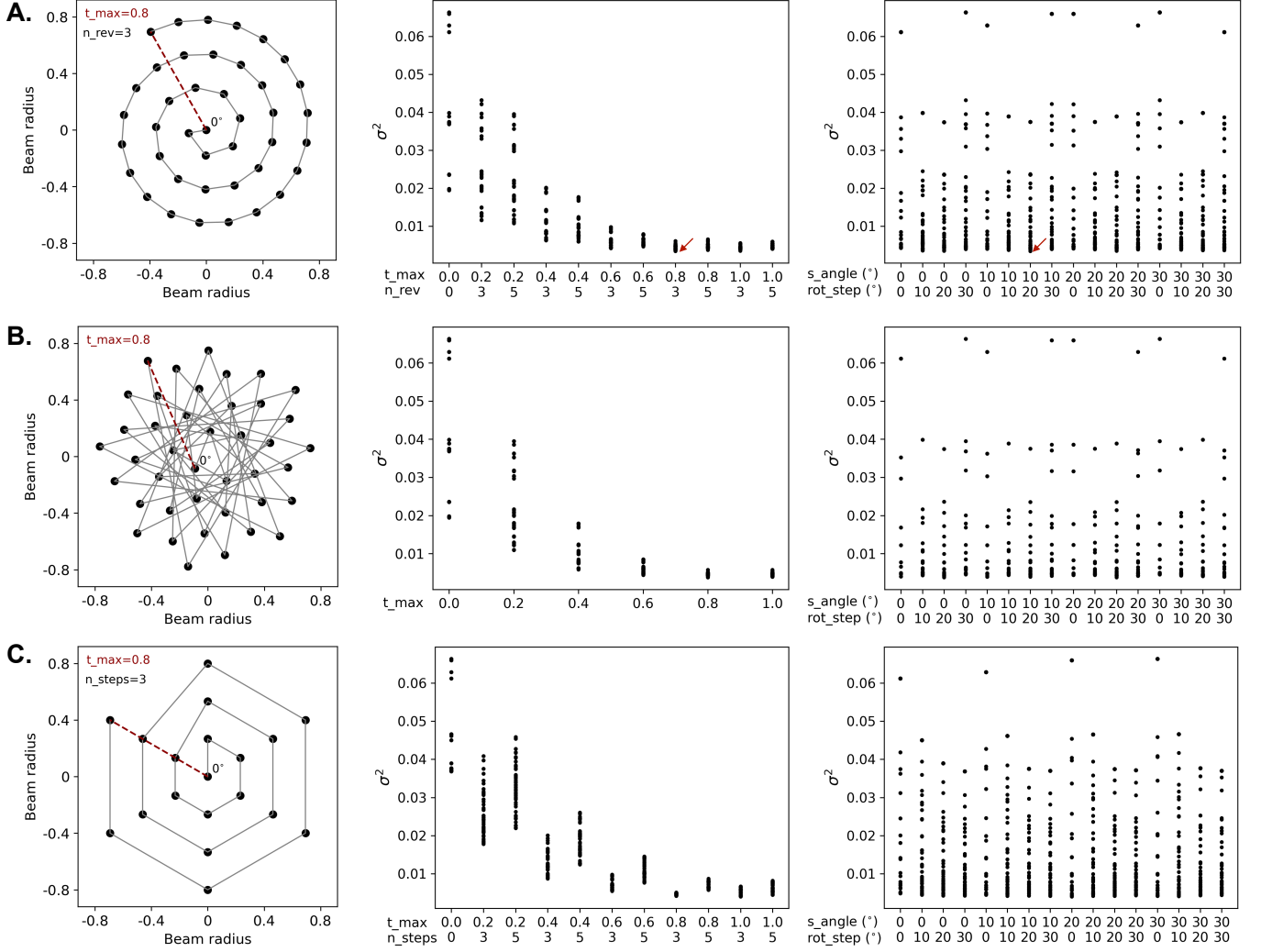


FIG. S3. **Tiling pattern efficiency is more sensitive to translational than rotational offsets between tilt angles.** The changes in the position of the central tile between tilt angles for the (A) Archimedean spiral, (B) sunflower, and (C) snowflake patterns are shown at left. For each pattern, the position of the central tile at the first tilt angle of 0° is noted, and its position follows an outward spiral (indicated by the grey line) during the tilt-series. For the snowflake pattern, the original pattern is repeated after the outermost point is reached. Translational parameters are noted at the upper left. For each, t_{max} (red line) indicates the maximum displacement of the central tile during the tilt-series. The parameters n_{rev} and n_{steps} correspond to the number of revolutions and radial steps for the spiral and snowflake patterns, respectively. Variants of each spiral pattern were simulated and ranked based on the variance (σ^2) of the normalized dose distribution. Variance scores are shown as a function of the indicated translational parameters (center) and rotational parameters (right). For the latter, parameters s_{angle} and rot_{step} respectively refer to the initial angular offset of the hexagonally-packed tiles in the plane of the detector and the global rotation applied between tilt angles. Simulations were performed using a tilt-range of $\pm 60^\circ$ with 3° increments between tilts, applying a $1/\cos$ exposure scheme, and assuming that Fresnel fringes contaminated 2% of the beam radius. The red arrows in (A) indicate the top-ranked pattern.

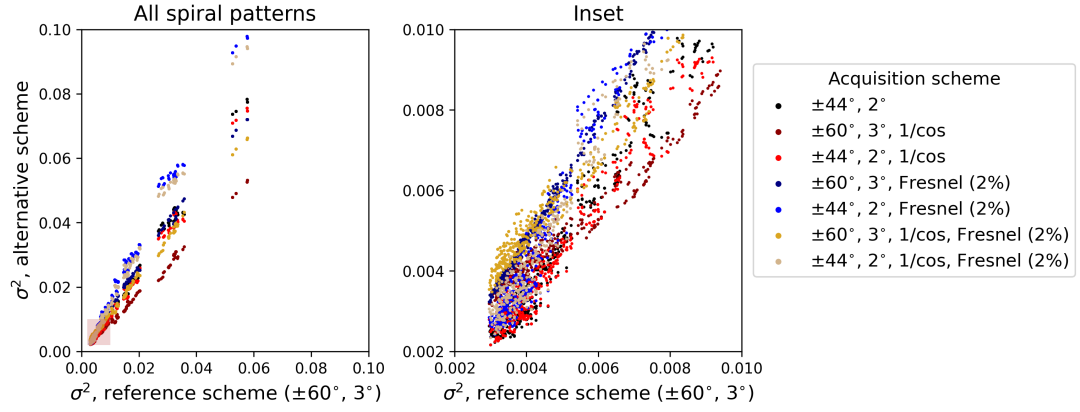


FIG. S4. **Tiling strategy efficiency is similar across different data collection schemes.** 546 unique variants of the spiral pattern were tested and scored by the variance (σ^2) of the accumulated dose distribution. The score of each pattern for the indicated data acquisition scheme is compared to its score for a reference data collection strategy of $\pm 60^\circ$ with 3° increments between tilt angles. Alternative acquisition schemes used a tilt-range of $\pm 44^\circ$ with 2° increments between tilt angles, increased the dose as $1/\cos$ of the tilt-angle, and/or increased the overlap between neighboring tiles to account for Fresnel fringes spanning 2% of the beam's radius. The transparent pink box overlaid on the highest-ranked patterns (left) is shown in the inset (right).

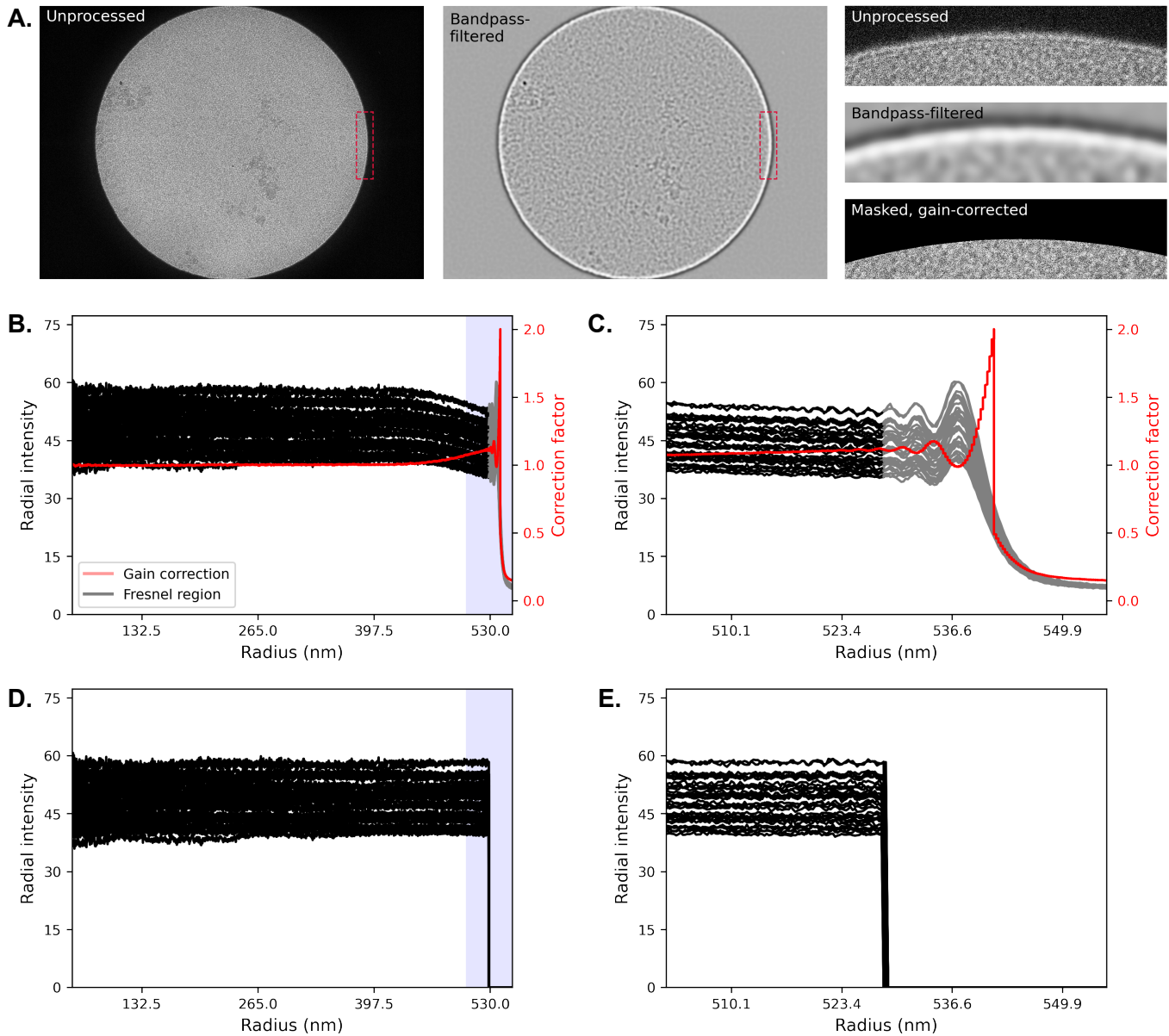


FIG. S5. Removal of the fringe-corrupted region and correction for uneven radial illumination. (A) A representative tile is shown before (left) and after (center) applying a bandpass filter. In the filtered tile, a high intensity ring (white) coincides with the Fresnel fringes at the tile's edge. (Right) The region boxed in red from the unprocessed, bandpass-filtered, and masked tiles visualizes elimination of the Fresnel fringes. (B) Radial intensity profiles for all 37 tiles from a representative tilt angle are plotted in black, with the region judged to be corrupted by Fresnel fringes plotted in grey. The radial gain factor used to correct uneven illumination is plotted in red. (C) Inset of the shaded blue region in (B) that focuses on the edge of the tiles affected by Fresnel fringes. (D) Radial intensity profiles of these tiles after correcting for uneven radial illumination and masking the fringes and (E) the corresponding inset.

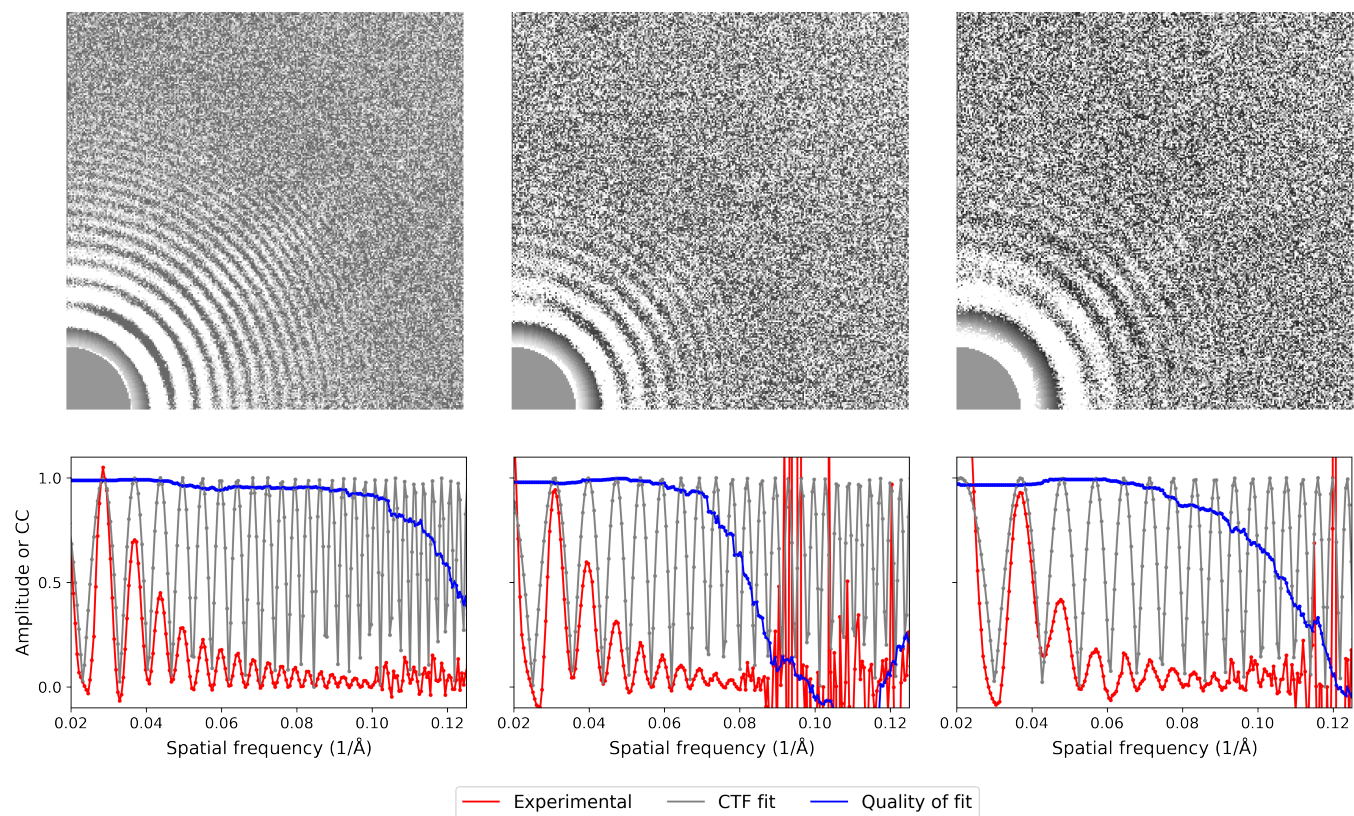


FIG. S6. **CTFFIND4 detects Thon rings to 8-12 Å in the untilted stitched projection images.** The 2D experimental spectrum (upper) and rotationally-averaged 1D CTF fits (lower) are shown for the CTF-uncorrected stitched projection images collected at 0° from three different tomograms. The leftmost plots are also shown in Fig. 2B but are reproduced here for comparison.

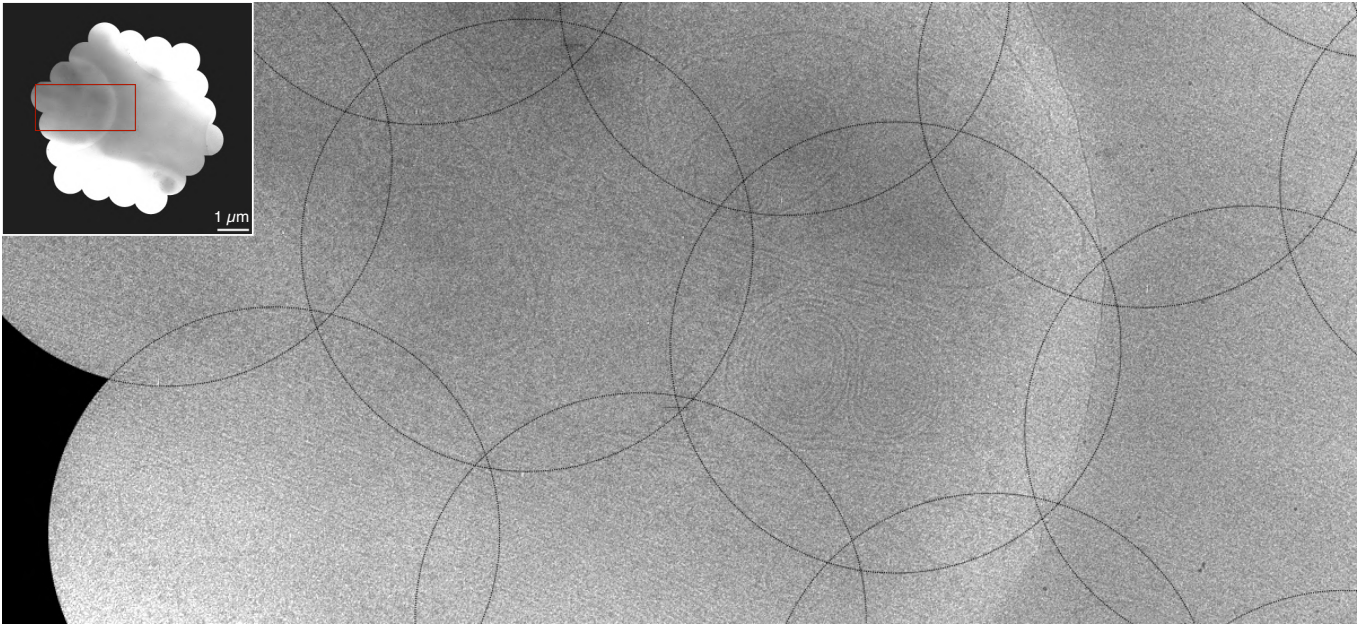


FIG. S7. **Continuous cellular features are observed in the overlap regions at intermediate tilt angles.** As in Fig. 3, except the stitched tiles imaged at 30° are visualized. The inset displays the full mosaic prior to cropping for reconstruction. The region boxed in red is enlarged in the main image. The boundaries of the $1.08 \mu\text{m}$ diameter circular tiles are outlined in black. The continuity of membrane features in the overlap regions between adjacent tiles suggests minimal radiation damage, even at an intermediate stage of data collection.

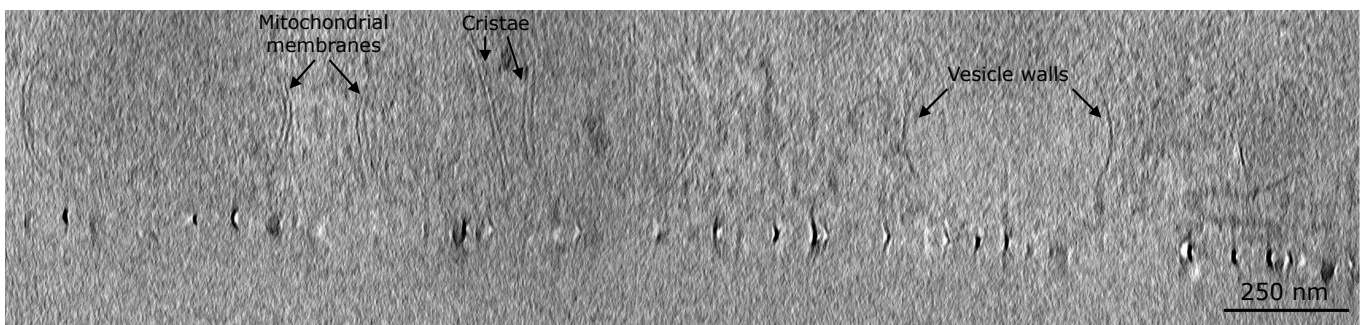


FIG. S8. **Continuous cellular features in an orthoslice from a montage tomogram.** An orthoslice from the tomogram presented in Fig. 4 is shown, with cellular features annotated.

Movie S1. **Representative montage cryo-tomogram featuring vesicles, actin bundles, and mitochondria.** Slices along the z -axis are scanned for the tomogram displayed in Fig. 4, with a $3.3 \mu\text{m}^2$ field of view.

Movie S2. **Inset of a representative montage cryo-tomogram featuring vesicles, actin bundles, and mitochondria.** Close-up of a portion of the tomogram shown in Movie S1; the scale bar indicates 200 nm.

Movie S3. **Representative montage cryo-tomogram featuring microtubules and multilamellar vesicles.** Slices along the z -axis are scanned for a second example montage cryo-tomogram, with a $3.3 \mu\text{m}^2$ field of view.

Movie S4. **Inset of a representative montage cryo-tomogram featuring microtubules and multilamellar vesicles.** Close-up of a portion of the tomogram shown in Movie S3; the scale bar indicates 200 nm.

Movie S5. **Representative montage cryo-tomogram featuring vesicles, microtubules, and ribosomes.** Slices along the z -axis are scanned for the tomogram displayed in Fig. 5, with a $3.3 \mu\text{m}^2$ field of view.

Movie S6. **Inset of a representative montage cryo-tomogram featuring vesicles, microtubules, and ribosomes.** Close-up of a portion of the tomogram shown in Movie S5; the scale bar indicates 200 nm.